Numerical Simulation of Boundary Layer Structure and Cross-Equatorial Flow in the Eastern Pacific*

R. JUSTIN SMALL

International Pacific Research Center, School of Ocean and Earth Science and Technology, University of Hawaii, Honolulu, Hawaii

SHANG-PING XIE AND YUQING WANG

International Pacific Research Center and Department of Meteorology, School of Ocean and Earth Science and Technology, University of Hawaii, Honolulu, Hawaii

STEVEN K. ESBENSEN AND DEAN VICKERS

College of Oceanic and Atmospheric Sciences, Oregon State University, Corvallis, Oregon

(Manuscript received 17 December 2003, in final form 29 September 2004)

ABSTRACT

Recent observations from spaceborne microwave sensors have revealed detailed structure of the surface flow over the equatorial eastern Pacific in the boreal fall season. A marked acceleration of surface wind across the northern sea surface temperature (SST) front of the cold tongue is a prominent feature of the regional climate. Previous studies have attributed the acceleration to the effect of enhanced momentum mixing over the warmer waters. A high-resolution numerical model is used to examine the cross-frontal flow adjustment. In a comprehensive comparison, the model agrees well with many observed features of cross-equatorial flow and boundary layer structure from satellite, Tropical Atmosphere Ocean (TAO) moorings, and the recent Eastern Pacific Investigation of Climate Processes (EPIC) campaign. In particular, the model simulates the acceleration across the SST front, and the change from a stable to unstable boundary layer. Analysis of the model momentum budget indicates that the hydrostatic pressure gradient, set up in response to the SST gradient, drives the surface northward acceleration. Because of thermal advection by the mean southerly flow, the pressure gradient is located downstream of the SST gradient and consequently, divergence occurs over the SST front, as observed by satellite. Pressure gradients also act to change the vertical shear of the wind as the front is crossed. However, the model underpredicts the changes in vertical wind shear across the front, relative to the EPIC observations. It is suggested that the vertical transfer of momentum by mixing, a mechanism described by Wallace et al. may also act to enhance the change in shear in the observations, but the model does not simulate this effect. Reasons for this are discussed.

1. Introduction

The climatological state of the eastern equatorial Pacific is important to climatic variability such as the El Niño–Southern Oscillation. Coupled ocean–atmosphere models have difficulty modeling this state correctly (Mesocho et al. 1995; Davey et al. 2002) and hence studies of the physical processes of the air–sea interaction in the eastern equatorial Pacific are important [Cronin et al. 2002; see Xie (2004a) for a recent review]. In this paper, a high-resolution numerical model is used to investigate one component of the system, the response of the atmospheric planetary boundary layer (PBL) to the oceanic cold tongue and the sharp SST front on its northern edge. These numerical results are complementary to EPIC2001, an intensive observational campaign conducted during September and October 2001 as part of the Eastern Pacific Investigation of Climate Processes (EPIC; Cronin et al. 2002; Raymond et al. 2004).

At least two processes are conceivably important to the cross-equatorial flow in the eastern equatorial Pacific. First, air parcels flowing toward the equator cannot adjust to the change in Coriolis force and so advective accelerations become important. Mahrt (1972)

* International Pacific Research Center Contribution Number 299 and School of Ocean and Earth Science and Technology Contribution Number 6497.

Corresponding author address: Dr. R. Justin Small, International Pacific Research Center, School of Ocean and Earth Science and Technology, 2525 Correa Rd., University of Hawaii, Honolulu, HI 96822.
E-mail: small@hawaii.edu

noted that for a latitudinally constant pressure gradient, the meridional (cross isobar) velocity in the boundary layer was found to increase as the equator was crossed. The explanation was that for flow crossing the equator, the zonal wind component suddenly opposes the direction of the zonal Ekman wind, and flow is accelerated toward lower pressure (Mahrt 1972). Tomas et al. (1999) further noted that the meridional advection of anticyclonic absolute vorticity was important to cross-equatorial flow in their reduced gravity model. In particular, they found that the meridional advection of zonal momentum was essential to achieve a divergence/convergence couplet just north of the equator.

Second, in the eastern equatorial Pacific the low-level, large-scale southerly flow associated with the ITCZ and the Hadley cell is modified locally by the presence of the SST front, referred to here as the Equatorial Front. Observations from satellite show that the near-surface southeasterlies and southerlies are significantly accelerated (in a Lagrangian sense) as they cross the equatorial front (Fig. 1a; the wind speed changes 3 $m\,s^{-1}$ between 1°S and 2°N at 95°W, equivalent to a divergence of $0.9 \times 10^{-5}\ s^{-1}$ and an approximate Lagrangian acceleration of around $0.6 \times 10^{-4}\ m\,s^{-2}$ or 5 $m\,s^{-1}\,day^{-1}$). To explain the effect of SST gradients, Lindzen and Nigam (1987) proposed a boundary layer model where the eddy air temperature was positively correlated with the eddy SST throughout the layer, the eddy part being the deviation from zonal mean. In their model the sea level pressure anomalies overlie the SST anomalies. In low latitudes where the Coriolis force is negligible, the strongest winds would occur over the SST fronts in response to the pressure gradient.

Wallace et al. (1989) conducted an observational study of the effect of SST on surface winds in the eastern equatorial Pacific on seasonal and interannual time scales. They noted that the Lindzen–Nigam explanation was appropriate to the large-scale dynamics, but did not explain the fact that observations showed divergence over the SST front and the strongest winds located further north over warm water. Wallace et al. concluded that stability-induced mixing variations led to the precise phasing of the observed wind patterns. In particular, stable conditions over the cold tongue would lead to enhanced shear and a decoupling of weak surface winds from the higher level southeasterly jet. North and south of the cold tongue, unstable conditions exist and the vertical wind profile may be expected to be more uniform with stronger winds at the surface.

Recent findings from Tropical Atmosphere Ocean (TAO) buoy observations (Cronin et al. 2003) and numerical simulations (Small et al. 2003) of tropical instability waves have indicated that due to thermal advection, the PBL pressure gradient can be spatially lagged relative to SST gradient. This calls into question the hypothesis of Wallace et al. (1989) that pressure gradients cannot explain the observed SST–wind phase relationships in the eastern equatorial Pacific. These new findings suggest that a reexamination of the relative importance of pressure gradient, static stability variations, and momentum advection to the cross-equatorial flow is required.

The aim of this paper is to study atmospheric adjustment across the equator and SST front during the cold tongue season, using a high-resolution regional climate model. In particular, this paper will attempt to explain the structure of the PBL in the eastern equatorial Pacific based on numerical simulations and by comparison with observations from EPIC, TAO, and satellite. The findings will be interpreted in terms of the cross-equatorial momentum budget.

The paper is structured as follows: The numerical model, experimental setup, and the observations used for verification are presented in section 2. Section 3 discusses the mean states of the surface fields and of the boundary layer structure, both in model and in observations. Section 4 describes the effect of the thermal structure and thermal advection on the surface pressure gradients. In section 5, the model momentum budget is presented to explain the mechanisms of the cross-equatorial flow. Section 6 presents a discussion of how the present results compare with previous studies. Finally, section 7 presents conclusions of the study.

2. Numerical model and data

a. Numerical model and experimental details

The high-resolution regional climate model developed at the International Pacific Research Center (IPRC-RegCM) has been used to study the atmospheric response to the oceanic SST field. The IPRC-RegCM is a hydrostatic, sigma coordinate, primitive equation model (Wang et al. 2003; Small et al. 2003). The model was chosen as having detailed PBL and cloud physics parameterizations and high resolution. Details of the physical processes of the model are contained in Table 1, together with references and comments relevant to the simulation.

The model has 29 vertical levels with substantial high-resolution in the PBL (12 levels below 800 hPa).[1] In this study, the model domain extended from 15°S to 20°N, 130° to 63°W, with a grid spacing of ⅓°, both in zonal and meridional directions. The time step was 360 s. The model was run for a period from 1 September 2001 to 31 October 2001, chosen to correspond to the EPIC2001 field campaign (see section 2b). The first week was treated as a model spinup and so the model analysis used the last 54 days of data, which will be referred to as "two months" for simplicity later on.

The turbulence scheme follows the Langland and

[1] The model sigma levels are: 0.0, 0.03, 0.05, 0.07, 0.09, 0.11, 0.14, 0.18, 0.24, 0.3, 0.37, 0.44, 0.51, 0.58, 0.65, 0.72, 0.77, 0.81, 0.84, 0.862, 0.882, 0.902, 0.92, 0.938, 0.956, 0.972, 0.988, 0.994, 1.

TABLE 1. List of physics parameterization schemes used in the IPRC-RegCM (version 1.1).

Physical process	Scheme	Reference	Comments
Grid-resolved moist processes	Bulk mixed ice phase cloud microphysics	Wang (1999, 2001) and references therein	
Subgrid-scale convection	Shallow convection, midlevel convection, and deep convection	Tiedtke (1989), Nordeng (1994), Gregory et al. (2000)	With CAPE closure and organized entrainment and detrainment. Coupling between subgrid-scale convection and grid-resolved moist processes via cloud-top detrainment (Wang et al. 2003).
Mixing	Vertical: 1.5-level turbulence closure	Langland and Liou (1996), Detering and Etling (1985)	Modified to include cloud buoyancy production of turbulence (Wang 1999).
	Horizontal: Fourth-order	Wang et al. (2003)	Deformation and terrain-slope dependent diffusion coefficient.
Surface layer over ocean	Bulk scheme	Fairall et al. (1996)	TOGA COARE v2.6
Radiation	Multiband	Edwards and Slingo (1996) updated by Sun and Rikus (1999)	7 bands for longwave, 4 bands for shortwave. Full coupling between cloud microphysics and cloud liquid/ice water path.
Cloud optical properties	Longwave radiation	Sun and Shine (1994)	
	Shortwave radiation	Slingo and Schrecker (1982), Chou et al. (1998)	With specified cloud droplet number concentration (CDNC) of 100 cm^{-3} over ocean and 300 cm^{-3} over land.
Cloud amount	Semi-empirical scheme	Xu and Randall (1996)	Dependent on relative humidity and cloud liquid/ice water extent.
Land surface processes	Biosphere–Atmosphere Transfer Scheme (BATS)	Dickinson et al. (1993)	Modified algorithm for solving leaf temperature to ensure a convergent iteration of numerical solution (Wang et al. 2003).

Liou (1996) 1.5-level closure, run with a separate time step of 120 s. Surface boundary conditions for this scheme are as formulated by Mailhot and Benoit (1982) and are dependent on the friction velocity u^* provided by surface layer theory. The surface layer in the model lies between the surface and the lowest sigma midlevel, ($\sigma = 0.997$, at around 30 m) and is assumed a constant flux layer. The bulk fluxes, u^*, and the roughness length z_0 are derived from the model data at $\sigma = 0.997$ and the known SST distribution, using the Fairall et al. (1996) surface layer algorithms. We derive the model neutral equivalent 10-m wind speed as follows:

$$u(z) = \frac{u^*}{\kappa}\left(\ln\frac{10}{z_0}\right), \quad (1)$$

where κ is von Kármán's constant.

The model atmosphere responds to a prescribed time-dependent SST, which in this case was a daily SST product derived from a three-day running mean of Tropical Rainfall Measuring Mission (TRMM) Microwave Imager (TMI) data, obtained from Remote Sensing Systems (www.ssmi.com). National Centers for Environmental Prediction–National Center for Atmospheric Research (NCEP–NCAR) reanalysis (Kalnay et al. 1996) version 3 products (released in May 2002) are used to initialize the model and to provide lateral boundary conditions every 6 h [see Wang et al. (2003) for details].

b. Observations

Model simulations in this study will be compared with data from the EPIC-enhanced monitoring program (Cronin et al. 2002) and the EPIC2001 intensive field campaign (Raymond et al. 2004). The EPIC dataset includes long time series of surface meteorological variables from TAO buoys at 95°W, enhanced with extra buoys at 3.5°N, 10°N, and 12°N. Here, measurements of basic meteorological quantities at the TAO moorings at typical heights of 4 m are converted to bulk fluxes using the Fairall et al. (1996) algorithm. The EPIC2001 intensive field campaign was conducted during September and October 2001, including ship and NCAR C130 aircraft measurements along transects at 95°W and at a fixed location under the ITCZ (Raymond et al. 2004). In this paper, data from the TAO moorings and NCAR C130 aircraft flights will be used.

Cross-equatorial flight transects along 95°W made on eight days between 7 September and 10 October 2001 are used to construct composite sections of cross-equatorial PBL structure. On the southward legs of these flights in situ measurements of various quantities including temperature, wind velocity, water vapor, cloud liquid water, and flux measurements were performed. The "porpoising," repeating flight pattern consisted of level flight legs (nominally 50 km in length) at 32 and 1628 m connected by ascent and descent periods with eight cycles over 13 degrees of latitude. On the

northward return, dropsondes were released at an altitude of 5.5 km at 1°-latitude intervals from the equator to 12°N. The soundings from the dropsondes were combined with the low-level flight legs to create latitude–height cross sections. Further information on the flight measurements can be found in McGauley et al. (2004).

Turbulent fluxes were measured using correlations of turbulent quantities, sampled at 25 Hz, equivalent to a 5-m range sampling along the flight track. Additional flux measurements were made during two NCAR C130 flights over the SST front on 3 and 5 October 2001, when the aircraft flew two stacks of east–west legs centered at 0.5°S and 2°N within 55 km of 95°W. For each flight day, the mean and standard error of direct estimates of the momentum flux were computed at each vertical level for each location following the method of Vickers and Mahrt (2003). Although alongwind biases were found in the NCAR C130 wind stress measurements (C. Bretherton 2004, personal communication), the east–west legs avoid much of the difficulty since the mean winds during the flights had a relatively large southerly component.

In addition to the in situ data, observations from the QuikSCAT and TRMM satellites were obtained from Remote Sensing Systems (www.ssmi.com). The data provided is gridded onto ¼°, and for a three-day running average. The QuikSCAT scatterometer is used to provide measurements of surface stress and derived 10-m neutral equivalent vector wind (Wentz and Smith 1999). The TMI data was used to provide descriptions of the SST field.

3. Mean state

a. Near-surface fields

A time mean was constructed from the two months of the model simulation to indicate the background flow field. Figure 1b shows the observed SST and modeled neutral equivalent wind speed and vectors at 10 m. The situation is typical of the eastern equatorial Pacific in the boreal fall season in non–El Niño years when the cold tongue is particularly prominent (Wallace et al. 1989).

The modeled 10-m neutral winds in Fig. 1b may be compared with the observed QuikSCAT winds for the same period (Fig. 1a). The cross-equatorial flow, meridional shear of zonal velocity, and convergence into the ITCZ at around 10°–12°N is reproduced reasonably well in the model. In contrast, the low wind speed core of 4–6 m s^{-1} in the model over the cold tongue (Fig. 1b) has a much smaller zonal extent than in the observations (Fig. 1a). Further, the high wind speeds a few degrees poleward of the cold tongue are about 1 m s^{-1} higher in the model than in the observations. Thus, the simulated wind speeds are higher overall than observed by QuikSCAT. (The IPRC-RegCM also simulated higher wind speeds than the NCEP–NCAR reanalysis data used to force the model, suggesting that the bias was not due to the forcing.)

Despite the absolute difference between the model and QuikSCAT wind speeds, the divergence fields, which are a relative measure, are similar (Figs. 2a, b). One distinct feature in these fields is the strong divergence located precisely over the equatorial front. This contrasts with a weak convergence south of the cold tongue (more prominent in the observations, Fig. 2a) and strong convergence in the ITCZ.

The two-month mean of near-surface quantities from the model data at 95°W is next compared with data from the TAO mooring array and QuikSCAT data at the same longitude and period and with in situ turbulent flux and related statistics from an eight-flight composite of the NCAR C130 data at the lowest flight level (between 25 and 30 m, see section 2b).

The ocean–atmosphere interface is typically unstable in the eastern equatorial Pacific. The modeled air–sea virtual potential temperature difference ($S = \theta_{vs} - \theta_{va}$, where subscripts a and s refer to air and sea, respectively, and the virtual temperature in the model at 30-m height was used to compute θ_{va}) shows positive values of S everywhere except for near the center of the cold tongue, and rising to a peak over 4 K, just north of the equatorial front (Fig. 3a). Over the cold tongue the interface is weakly stable or close to neutral stability with minimum S between –0.5 and –1 K. The strong meridional gradient in S across the equatorial front shows that as the air passes across the front it is rapidly destabilized. The TAO values of virtual air–sea temperature difference (S) show a very similar range to that seen in the model in the region of the equatorial front (Fig. 3b).

The changes in stability lead to large variations in heat fluxes across the front. The modeled sensible heat rises from –3 W m^{-2} over the cold tongue to a peak of 37 W m^{-2} close to 2°N, somewhat higher than the peak of around 29 W m^{-2} in the TAO and C130 flight data (Fig. 3c). The modeled latent heat flux rises from 20 W m^{-2} to a peak comparable with the C130 data (200 W m^{-2} between 2° and 3°N) but rather larger than the TAO value (peaking at 140 W m^{-2}; Fig. 3e).

Comparisons of the surface wind stress indicate that the model values are larger than the measurements from TAO and QuikSCAT (by around 0.01–0.02 N m^{-2}, or about 20%–50%, Fig. 3b) but that the relative difference between 1°S and 2°N is similar (0.05 N m^{-2}), suggesting that the model captures the change in stress across the front. The overall larger stress (and hence u^*) in the model data, related to the larger wind speeds noted in Fig. 1, may also explain why the sensible and latent heat, which depend on u^*, are larger than observed.

The model values of near-surface turbulent kinetic energy (TKE), Fig. 3d, are also larger than the EPIC2001 data (by around 0.03–0.05 m^2 s^{-2}, about 20%–50%), partly due to the larger values of u^* in the

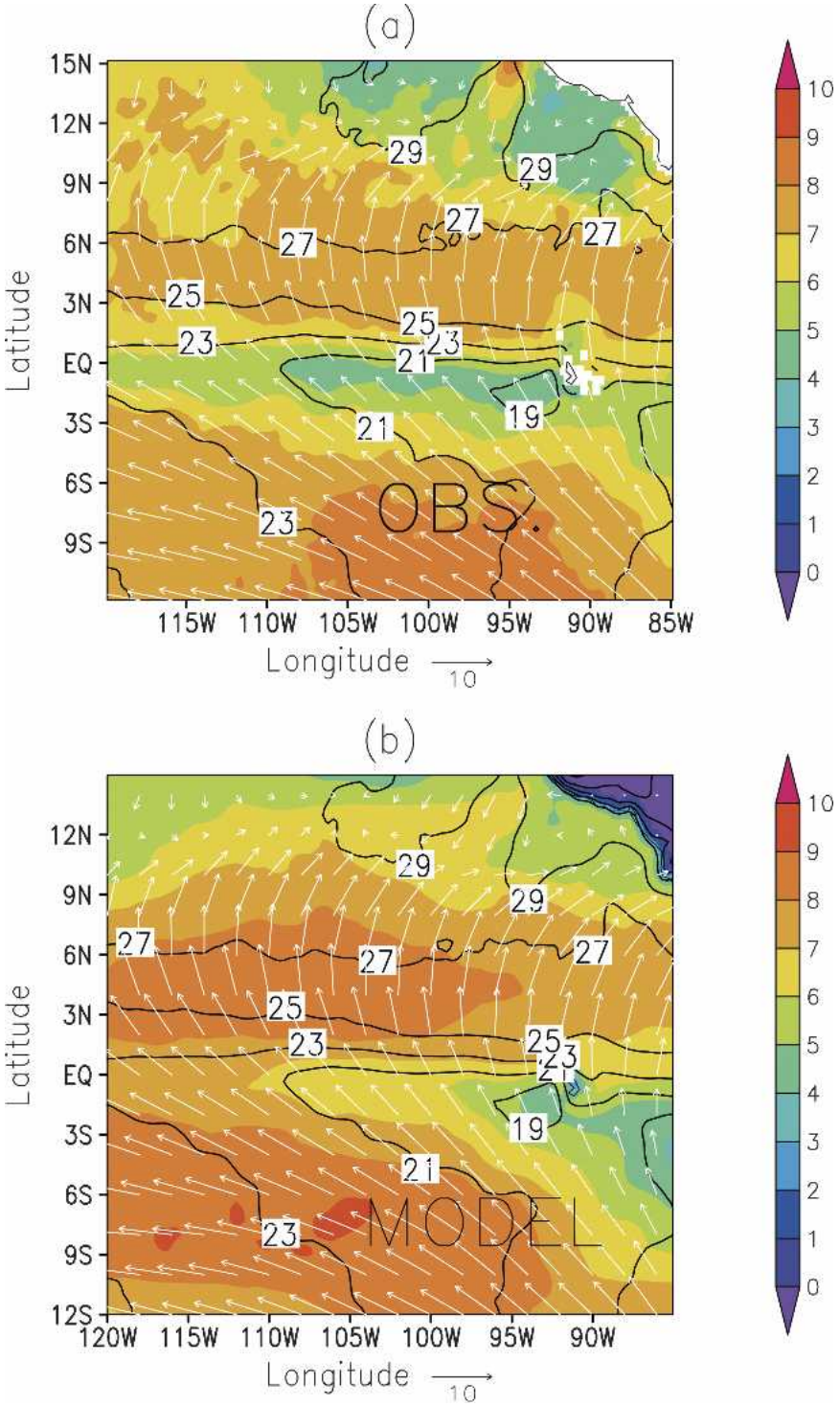

FIG. 1. Neutral equivalent 10-m mean wind speed (color, m s^{-1}), vectors (m s^{-1}, see scale arrow), and SST (°C, line contours) in the eastern equatorial Pacific for a 2-month time mean, Sep–Oct 2001. (a) Wind observations from QuikSCAT and SST from TMI, and (b) model simulation of winds for the same time period, together with TMI SST.

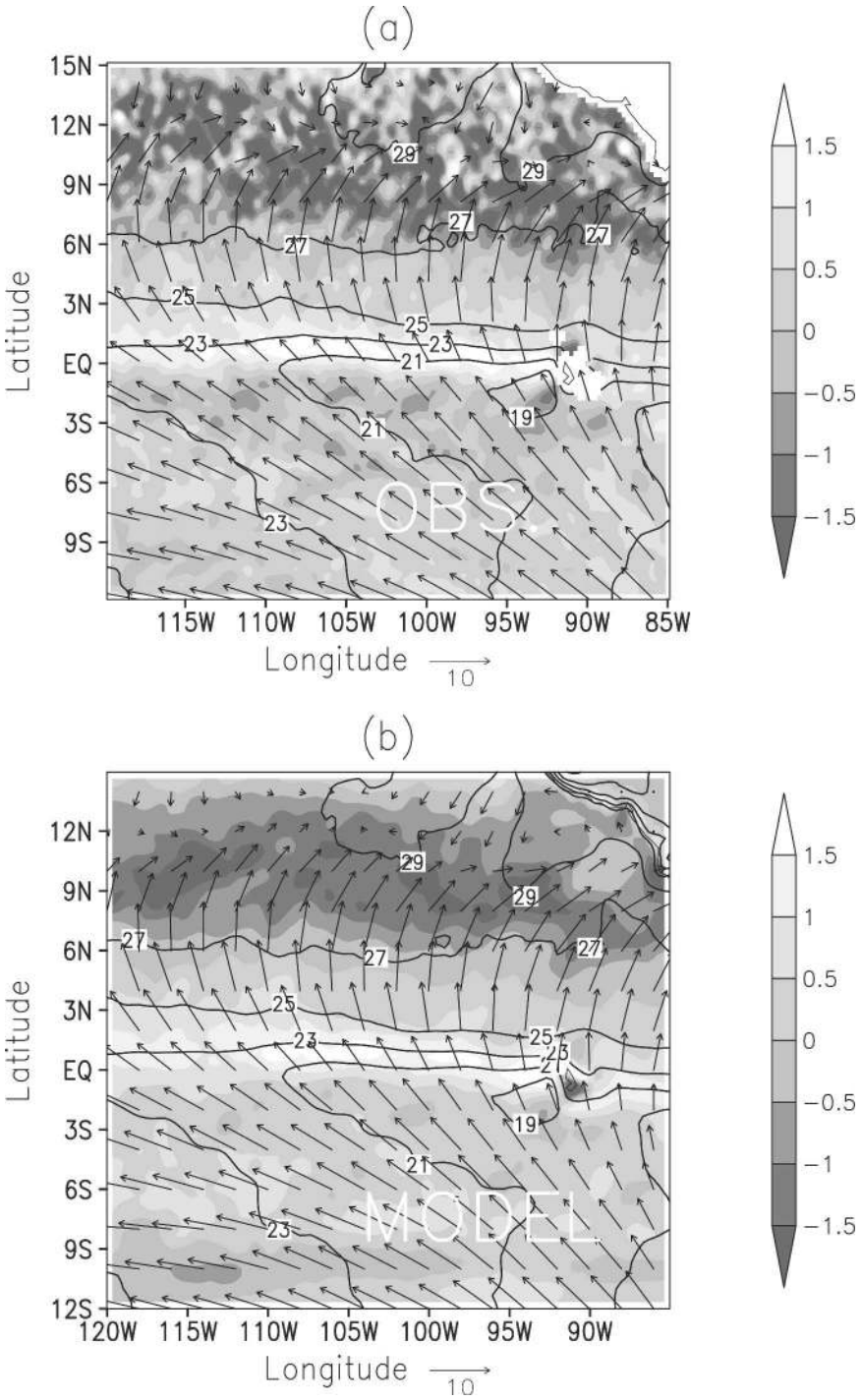

FIG. 2. Divergence of neutral equivalent 10-m mean wind (10^{-5} s^{-1}, grayscale), SST (°C, line contours), and wind vectors (m s^{-1}, see scale arrow) for a 2-month time mean, Sep–Oct 2001. (a) Observed from QuikSCAT and TMI, and (b) modeled divergence and TMI SST.

model [the lower boundary condition on TKE in the model is dependent on u^* (Mailhot and Benoit 1982)] but again the difference across the front is comparable in model and data. (TKE was calculated from the C130 vertical velocity variance data by assuming isotropic turbulence, so that TKE $\cong 1.5\ \overline{w'^2}$.)

Note that besides model deficiencies, differences between the measurements and model may arise due to

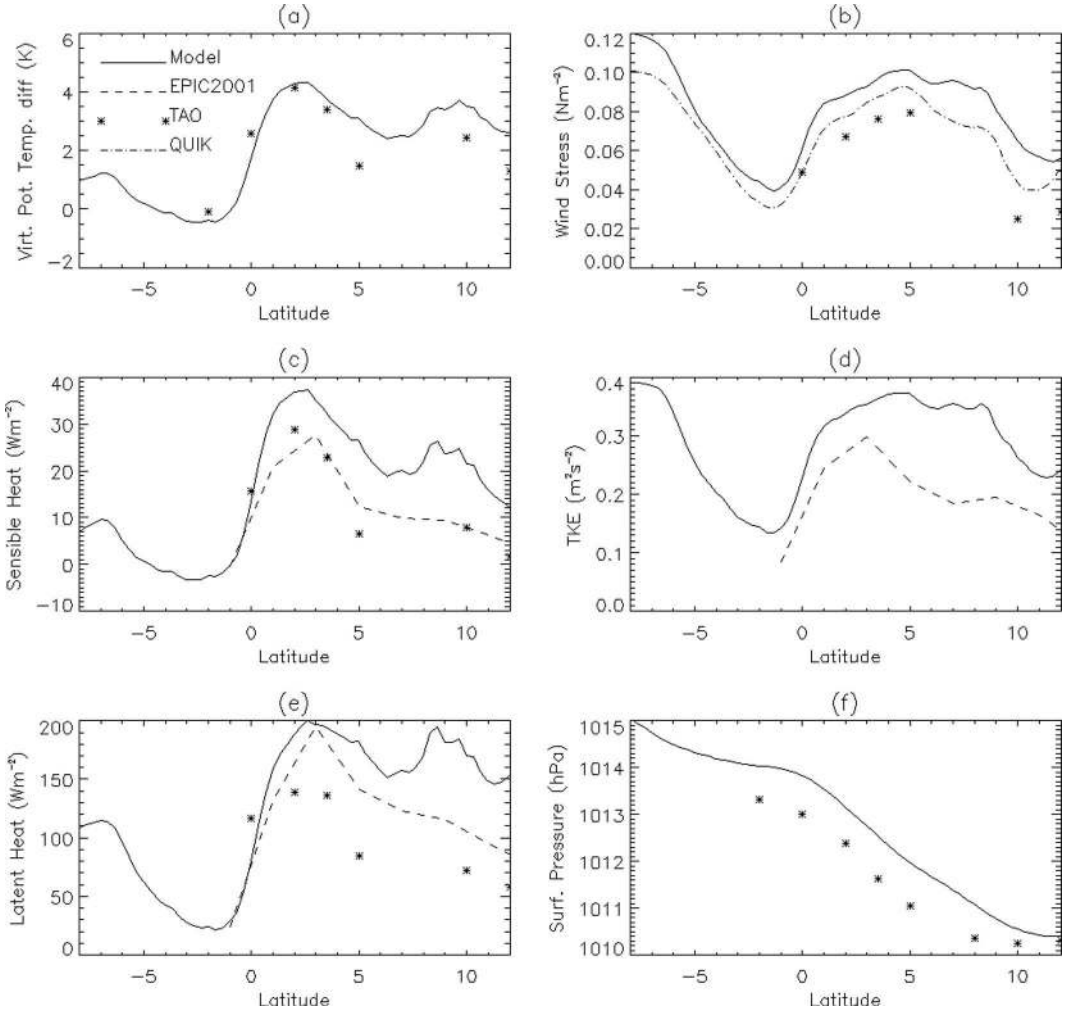

FIG. 3. Comparison of surface quantities at 95°W from model and observed data from the eight-flight NCAR C130 composite (EPIC2001), QuikSCAT, and TAO mooring data (see legend). (a) Virtual potential air − sea temperature difference (K), (b) wind stress (N m^{-2}), (c) sensible heat flux (W m^{-2}), (d) turbulent kinetic energy (m^2 s^{-2}), (e) latent heat flux (W m^{-2}), and (f) surface pressure (hPa). Model, QuikSCAT, and TAO data are a 2-month time mean.

several factors: First, the difference between direct turbulent correlation methods used by the NCAR C130 instrument as compared to the bulk fluxes used for the model and TAO data; second, data sparseness (very little TAO wind speed data was gathered in September at 95°W between 2°S and 2°N, explaining the lack of bulk heat flux values there, and the NCAR C130 data was gathered on just eight days); third, the different sampling strategies since TAO measurements are at a single position, the NCAR C130 flight survey followed a single vertical cross section, whereas the model simulations relate to a ⅓° grid box.

b. Planetary boundary layer structure

The model simulations of PBL vertical structure may be compared with NCAR C130 measurements from the EPIC2001 campaign. The model data is shown from 12°S to 12°N in Figs. 4a–6a while the EPIC2001 flight data, which only covered 1°S to 12°N is shown directly below the model data in Figs. 4b–6b. Individual profiles from over the cold tongue and over the warm water are also shown in Figs. 4c and 6c for the model, and Figs. 4d and 6d for observations. The observations are a composite of the eight flights at 95°W of the NCAR C130, while the model results are an average of the eight days corresponding to the NCAR C130 flights and have been converted from σ to z coordinates.

Over the cold tongue there is weakly stable stratification up to 700 m in the model (Figs. 4a,c) and observations (Figs. 4b,d). Above this is a region of strong stratification around 800–1000 m. The region below this strong stratification is the PBL. As air crosses the Equatorial Front a mixed layer forms and rapidly deep-

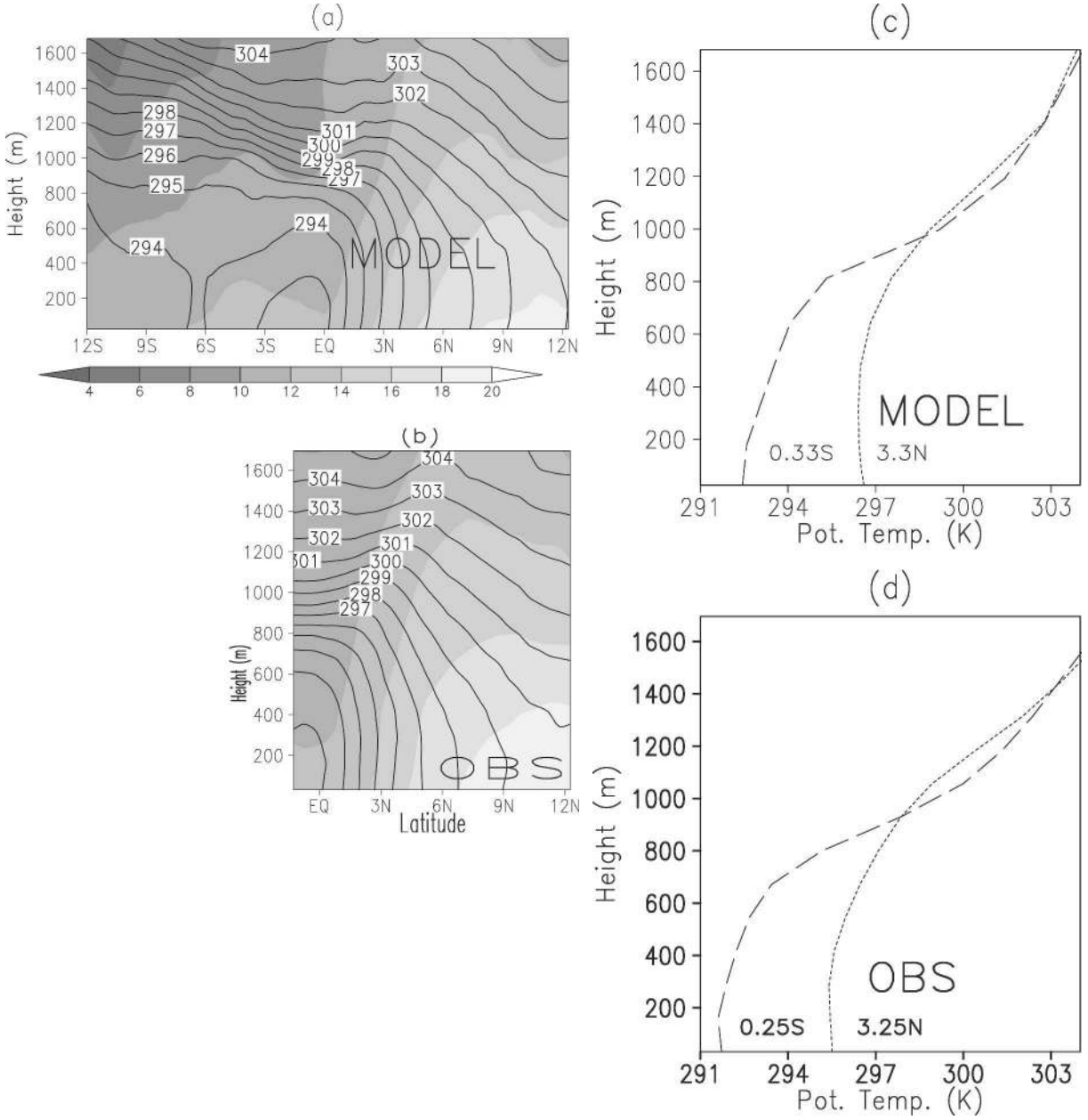

FIG. 4. Vertical sections at 95°W of water vapor mixing ratio (shaded, g kg^{-1}) and potential temperature (contours in K, with intervals of 1 K) (a) from the IPRC-RegCM, eight-day mean, and (b) from the EPIC2001 NCAR C130 data, eight-flight mean. (c) Vertical profile of potential temperature (K) from the model at 0.33°S and 3.3°N. (d) As in (c) but from observations at 0.25°S and 3.25°N.

ens in response to the heat fluxes and the mixing by turbulence, to an extent of about 300–500 m at 3°N, in model (Figs. 4a,c) and observations (Figs. 4b,d). Further, the mean potential temperature in that layer increases by 4 K relative to near-surface values over the cold tongue. Overall, the model near-surface temperatures are about 1 K warmer than observed (Fig. 4) for reasons unknown. Water vapor content (Figs. 4a,b, shaded) also increases to the north in the PBL by about 4 to 6 g kg^{-1} from the equator to ITCZ.

The warming, moistening, and deepening of the PBL in the model across the equatorial front leads to an approximately 1-hPa decrease in the surface pressure between 0° and 3°N, contrasting with the slow decrease of around 1 hPa between 8°S and 0° (Fig. 3f). (As discussed in section 5, this suggests that indeed the pressure gradient induced by the PBL changes is an important factor in determining the cross-equatorial acceleration.) The modeled sea level pressure was compared against measurements made on the enhanced TAO mooring array (Cronin et al. 2003): the modeled values are consistently higher than the data by about 0.5 hPa,

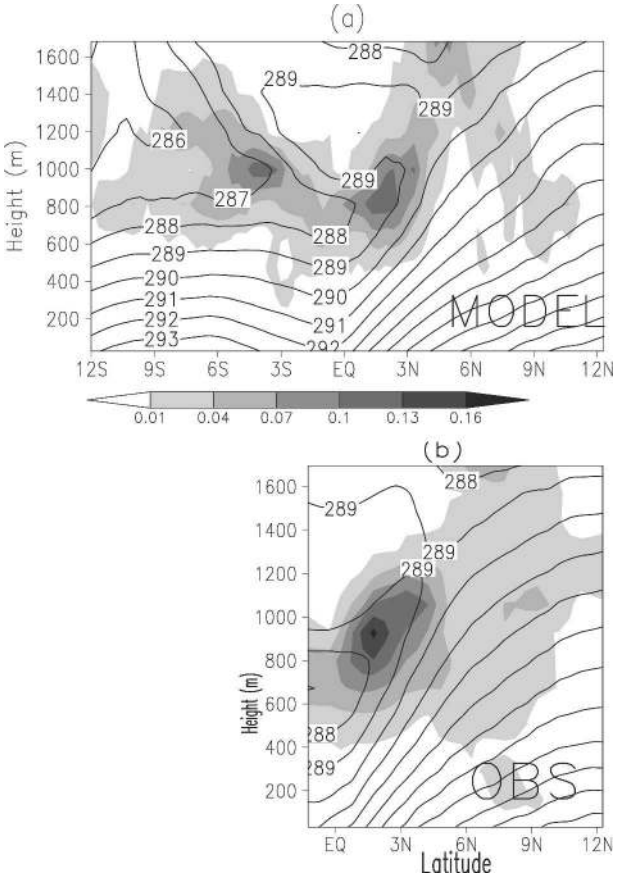

FIG. 5. Vertical sections at 95°W of cloud liquid water (shaded, g kg^{-1}) and temperature (contours in K, intervals of 1 K) (a) from the IPRC-RegCM, eight-day mean and (b) from EPIC2001 NCAR C130 data, eight-flight mean.

but the meridional gradient of pressure is similar (Fig. 3f, see also Fig. 8d below).

A temperature inversion exists in the southern latitudes and also extends as far as 2°–3°N in both model (Fig. 5a) and EPIC2001 observations (Fig. 5b), located between 700 and 1200 m height at 1°S. Clouds form at the base of this inversion. The cloud layer rises with increasing latitude northward from the equator, associated with the northern location of the ITCZ, the rise being more rapid in the model (Fig. 5a) than the observations (Fig. 5b). In both model and observations there is a local maximum of cloudiness between 1°N and 3°N. The maximum value of cloud liquid water is slightly higher in observations than in the model (by around 0.03 g kg^{-1}).

Wind speed and meridional wind sections at 95°W in the model (Fig. 6a) show that the highest wind speeds (white contours in Fig. 6a) occur in a boundary layer jet whose core lies between 300 and 600 m height south of the equator. The flow in this jet becomes more meridional as the equator is approached from the south. Over the cold tongue region (3°S to 0°) in the model the wind at the surface becomes decoupled from the upper-level jet. The meridional wind component at the surface at 0.33°S is 6.0 m s^{-1}, some 1.5 m s^{-1} less than in the jet at 400 m (Fig. 6c). In contrast, between 3° and 6°N the shear between the core and the surface is weaker (Fig. 6a): at 3.3°N the shear of meridional wind is 0.3 m s^{-1} between the surface and the jet, which has lowered to 200 m; Fig. 6c). Between 1°N and 3°N there is a small local minimum of wind speed at 300 m in the eight-day model mean (Fig. 6a). This feature was not present in the corresponding two-month mean (not shown) and is likely not significant.

The EPIC2001 flight data shows similar, but more marked, contrasts of wind structure across the equatorial front (Figs. 6b,d). Over the cold tongue, there is a shear of 1.8 m s^{-1} between the surface and the jet at 500 m in EPIC at 0.25°S (Fig. 6d), while at 3.25°N the meridional wind is completely uniform up to a height of between 200 and 300 m (Fig. 6d). It is also notable that the contrast in meridional wind and the associated horizontal divergence at the surface between the cold tongue and warm water is greater in the observations (2.4 m s^{-1} over 3.5°, Fig. 6d) than in the model (1.6 m s^{-1} over 3.7°, Fig. 6a). The reasons for the differences in magnitude of the change in vertical shear and of surface divergence will be discussed in section 6.

A map of the turbulent kinetic energy (TKE), Fig. 7, from the model at 95°W for the same eight-day mean indicates the mechanism of the change in PBL structure. High turbulence and buoyancy over the warmer waters gives rise to the deeper mixed layers, while weak turbulence over the cold tongue leads to the shallow mixed layer and a more stable profile. The vertical extent of influence of the TKE is smaller over the cold tongue than over the warm water. The latitudinal location of the maximum in TKE (2°–3°N) coincides with the region of highest virtual potential air–sea temperature difference S and of turbulent heat flux (Figs. 3a,c,e) where the static instability at the surface has given rise to buoyant turbulent eddies that are transported upward, resulting in the maximum of TKE higher in the PBL. The model TKE values are qualitatively similar to profiles of TKE inferred from EPIC2001 observations by de Szoeke et al. (2005) with a minimum over the cold tongue and a maximum between 2° and 4°N at 200–300-m height, but the magnitude of the model maximum (0.8 m^{-2} s^{-2}) is considerably larger than observed (0.3 to 0.4 m^{-2} s^{-2}), partly related to the larger surface fluxes in the model discussed in section 3a.

4. Effect of thermal advection on surface pressure gradients

a. Downstream location of the surface pressure gradient relative to the Equatorial Front

The changes in PBL thermodynamic structure across the equator, noted above, will lead to changes in sea

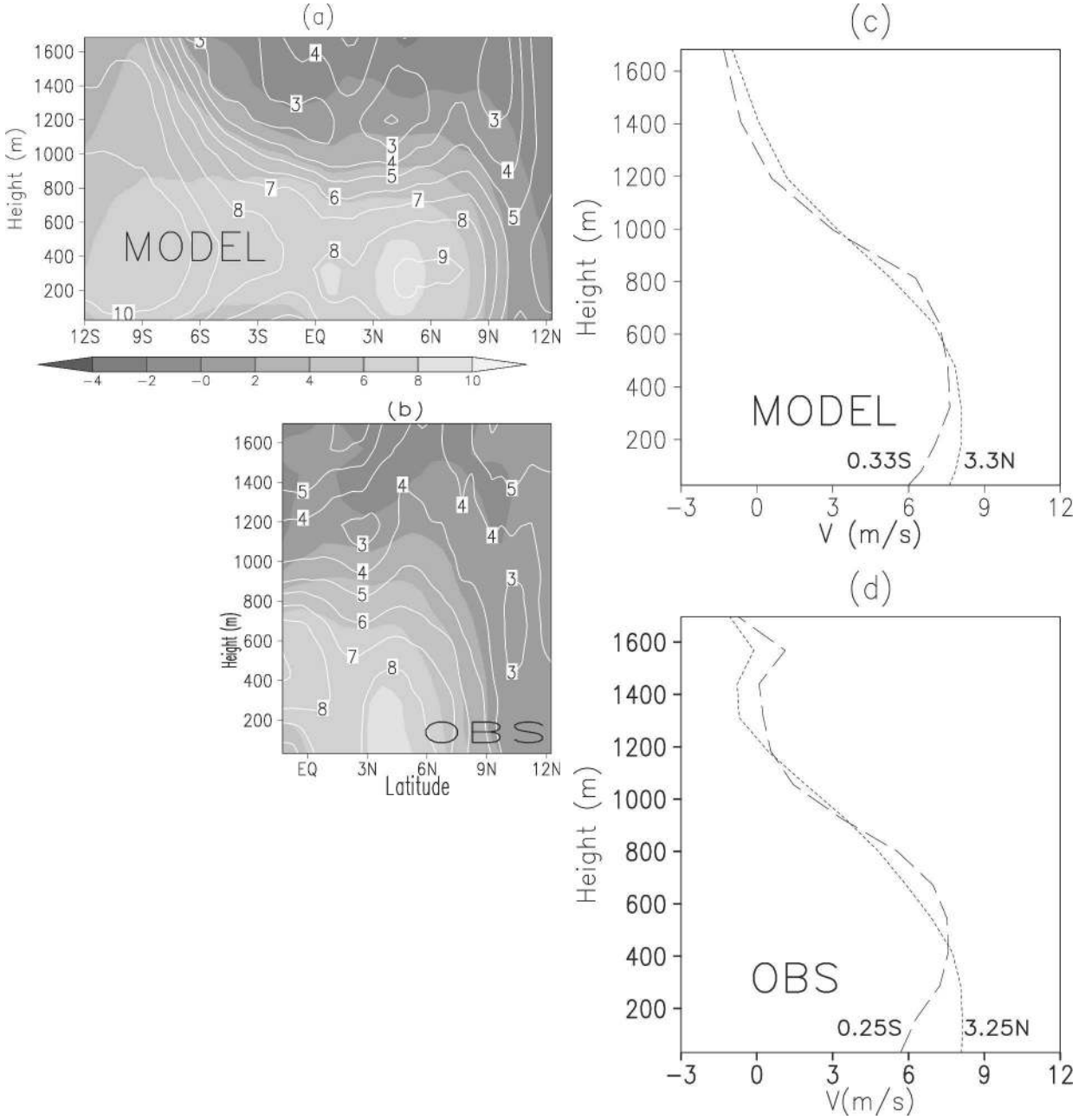

FIG. 6. Vertical sections at 95°W of meridional velocity (shaded, m s^{-1}) and wind speed (contours in m s^{-1}, intervals of 1 m s^{-1}) (a) from the IPRC-RegCM, eight-day mean and (b) EPIC2001 NCAR C130 data, eight-flight mean. Vertical profiles of meridional velocity (m s^{-1}) from (c) the model at 0.33°S and 3.3°N, and from (d) observations at 0.25°S and 3.25°N.

level pressure. Under the assumption that the gradients of SST and pressure are collocated (Lindzen and Nigam 1987), ocean frontal regions near the equator would be locations of highest pressure-driven wind speeds rather than of the largest wind divergence, as discussed by Wallace et al. (1989). However, a close examination of the gradients of surface pressure, SST, and virtual temperature T_v along 95°W suggests that the assumption of collocated SST and pressure gradients is not appropriate for the small frontal scales being considered here. Figure 8 shows the gradients derived from in situ data from TAO and EPIC NCAR C130 flights, compared to model data, and gradients derived from model data subsampled onto the TAO locations.

In general, the TAO and NCAR C130 gradient data support the model gradient values. At 95°W there is the large SST gradient of the Equatorial Front between 1°S and 1°N, peaking at around 0.3°N (Fig. 8a, solid line).

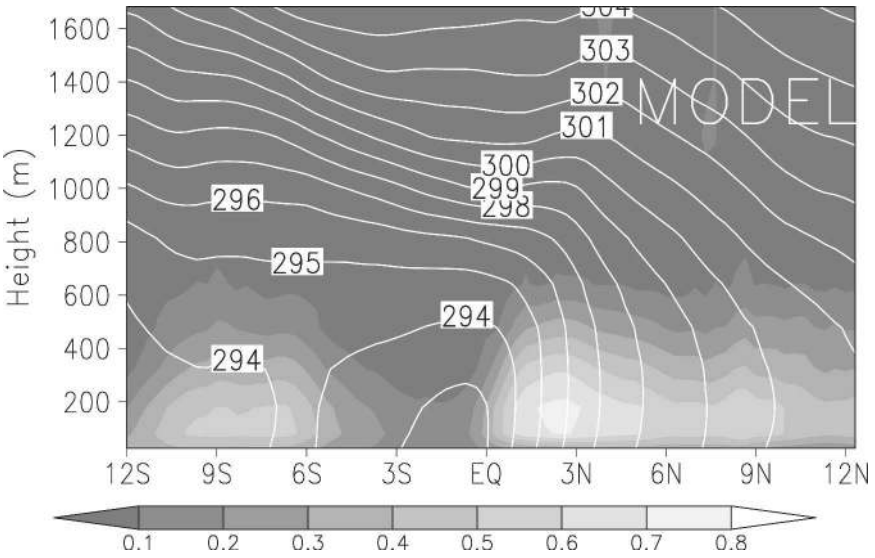

FIG. 7. Vertical section at 95°W from the model of TKE (shaded, $m^2\ s^{-2}$) and potential temperature (contours, K).

However, the pressure gradient reaches a peak some degrees north of this: at around 2° to 3°N in the model (Fig. 8d, solid line) and TAO data (Fig. 8d asterisks); when the model data is interpolated onto TAO locations, the peaks locations coincide closely (Fig. 8d, diamonds). This difference in location between the peak gradients of SST and pressure is due to the spatial lag of the air temperature adjusting toward the SST (see below). In fact, the largest gradients in near-surface virtual temperature T_v occur just north of the SST gradient peak and are spread over a wider extent than the peak in SST gradient in each of the model, TAO, and NCAR C130 data (Fig. 8b). The highest gradients in air temperature are also tilted northward with height (see Fig. 5), as can be seen by the peak positive gradient in T_v at 900–1000 m occurring at 3°–4°N in the model and NCAR C130 data[2] (Fig. 8c). (In fact, the NCAR C130 data shows a local reversed gradient near the equator, which would act to push the pressure gradient peak more downstream and northward.) Hence, the hydrostatic pressure gradients are also lagged downstream relative to the SST gradients, with a broad peak centered on 2°–4°N (Fig. 8d). McGauley et al. (2004) also found a maximum pressure gradient at a similar latitude (2°N for the pressure integrated over a 500-m mixed layer, their Fig. 4), using NCAR C130 flight-level data. They further showed that the gradient in surface pressure was primarily due to the gradient within the PBL, rather than the gradient in the pressure at the top of the PBL.

b. Temperature budget

The possibility that thermal advection is the cause of the downstream location of the surface pressure gradient is explored next using a heat budget analysis and a simple model.

The depth-averaged thermodynamic equation for temperature T in the boundary layer is given by (expressed in Cartesian coordinates for illustration)

$$\left\langle \frac{\partial T}{\partial t} \right\rangle = -\left\langle \mathbf{u} \cdot \nabla T + w \frac{\partial T}{\partial z} \right\rangle + \frac{F}{h} + \langle Q + \text{diff} \rangle, \tag{2}$$

where $\mathbf{u} = (u, v)$ is the horizontal velocity vector, w is vertical velocity, ∇ is the gradient operators, h is the averaging depth, $\langle \cdot \rangle = h^{-1} \int_0^h \cdot\, dz$, Q denotes adiabatic heating due to vertical motion, and diff denotes horizontal diffusion. The flux term F is composed of the surface sensible heat flux F_s, the flux at the top, F_h, and the radiative flux at surface and top, rad_s and rad_h:

$$F = F_s - F_h + \text{rad}_s - \text{rad}_h. \tag{3}$$

The variation of the dominant vertically integrated terms with latitude at 95°W is shown in Fig. 9a (the local tendency and horizontal diffusion were negligible and are not displayed). It can be seen that the vertical motion effects (vertical advection and adiabatic heating) mostly cancel, and the remaining balance is between the flux terms F (including both vertical diffusion and radiative flux) and the horizontal advection. The contribution of surface buoyancy F_s to the total flux F is

[2] Note that while the strongest T_v gradients occur in the PBL due to the surface forcing, a large-scale gradient is present over a very deep layer of the troposphere as a result of the deep condensational heat release in the ITCZ. This helps shift the top of PBL temperature maximum northward relative to the SST maximum (Fig. 8c).

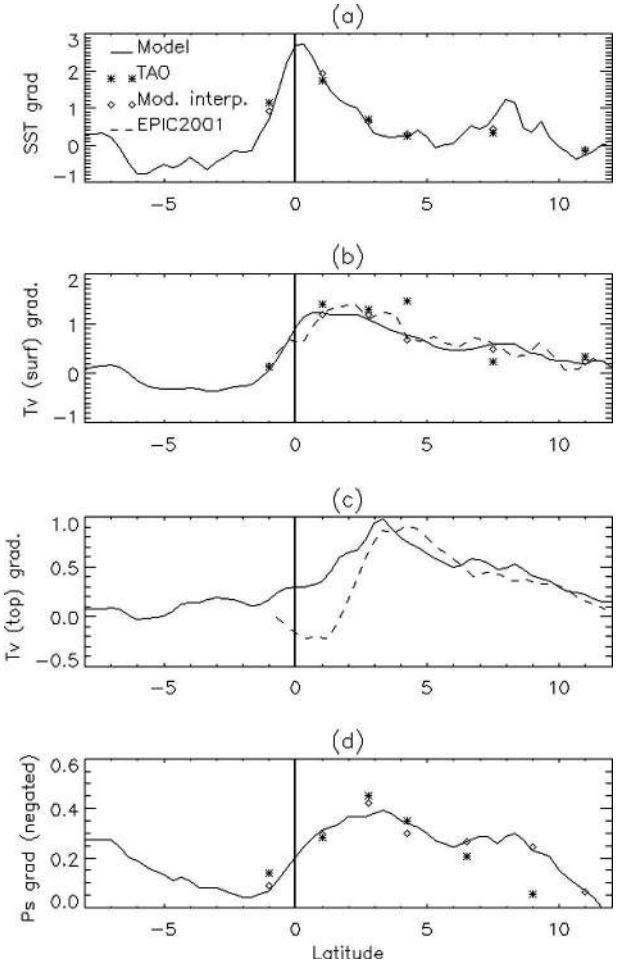

FIG. 8. Meridional gradients from model and observations, at 95°W from Sep to Oct 2001 of (a) SST [K (100 km)$^{-1}$], (b) near-surface virtual temperature [K (100 km)$^{-1}$], (c) virtual temperature for model σ level 0.911, and NCAR C130 altitude 928 m [K (100 km)$^{-1}$], (d) surface pressure, negated [hPa (100 km)$^{-1}$] from observed data from the eight-flight NCAR C130 composite (EPIC2001) and TAO mooring data (see legend). Gradients derived from model data sampled at TAO mooring positions are also shown. The thick vertical line marks the equator, close to the latitude of the peak SST gradient, for reference.

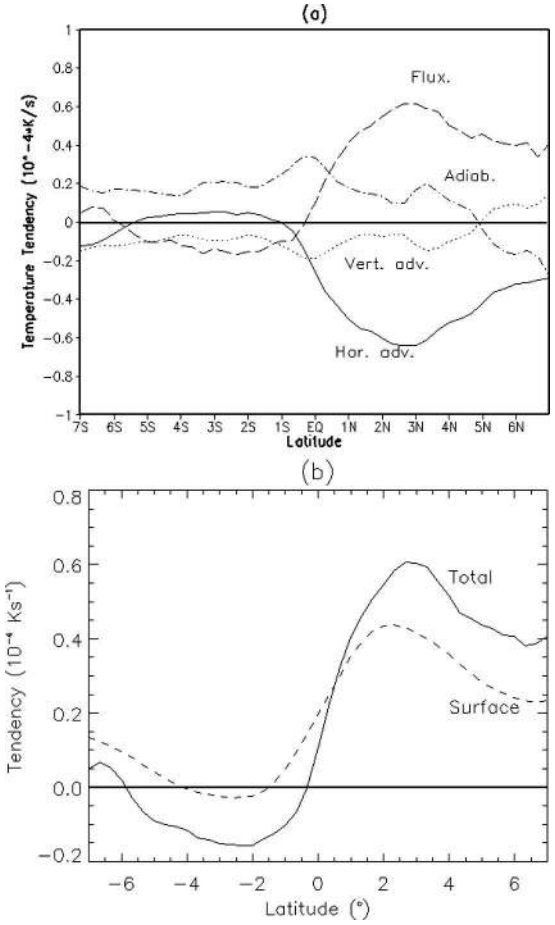

FIG. 9. (a) Vertically averaged temperature budget at 95°W, 2-month mean. All quantities are averaged (mass weighted) to 900 m, with units of 10^{-4} K s^{-1}. "Adiab." denotes adiabatic warming, "Hor. adv." denotes horizontal advection, "Vert. adv." is vertical advection, and "Flux" includes vertical mixing and radiative fluxes terms (see text). (b) Comparison of total flux and the surface sensible heating contribution. The zero line is marked for reference in (a) and (b).

dominant and explains most of the variation across the front as can be seen from Fig. 9b.

c. A simple model of thermal advection

Hence, we propose a simple illustration describing a balance between horizontal advection and surface heating. Further, we approximate the advection term of (2) by the horizontal advection by depth-mean meridional wind, giving

$$\left\langle v \frac{\partial T}{\partial y} \right\rangle \approx \langle v \rangle \cdot \left\langle \frac{\partial T}{\partial y} \right\rangle \approx \frac{1}{h} F_s, \tag{4}$$

where F_s is computed from the model sensible heat flux (Fig. 10a).

The change of $\langle T \rangle$ in the meridional direction at 95°W due to sensible heating is computed from (4), using finite difference with an initial value of $\langle T \rangle$ at 2°S in the cold tongue, taken from the full model results. The height for depth averaging, h, is kept constant at 900 m (which approximates the boundary layer height described in section 3a), and $\langle v \rangle$ is also taken from the model results. Denoting $\langle T_{es} \rangle$, the estimated depth-averaged T derived from (4) the resultant variation of $\langle T_{es} \rangle$ with latitude is shown in Fig. 10b (dashed line), which is compared with the value of $\langle T \rangle$ from the full model (Fig. 10b, solid line). Both $\langle T \rangle$ and $\langle T_{es} \rangle$ show similar warming trends with latitude, but the rate of increase is slightly higher in the full model, as seen in Fig. 10c, due to the contributions of F_h (entrainment) and other terms to the warming. The meridional temperature gradient displays a broad peak centered at

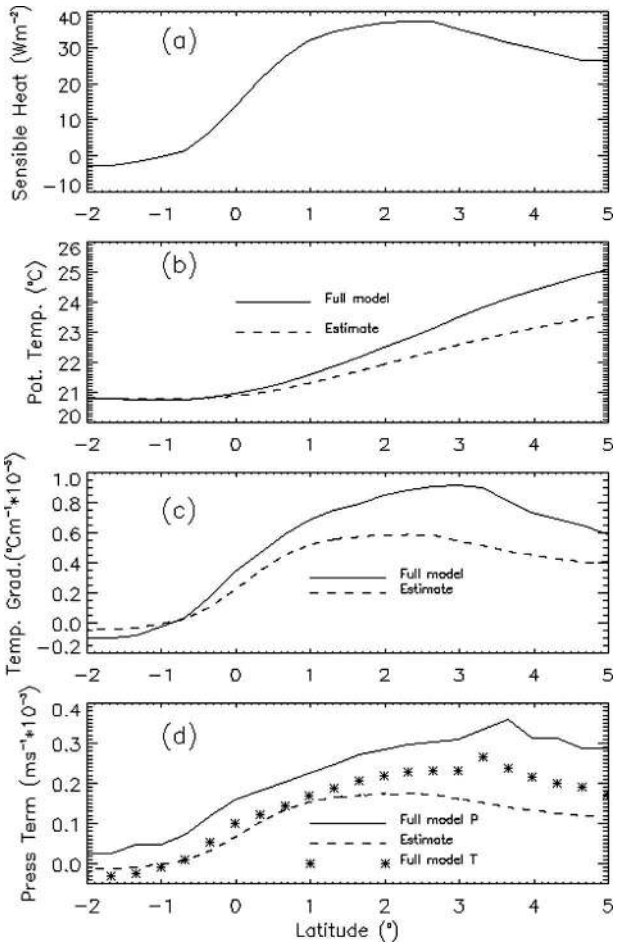

FIG. 10. Sections at 95°W from full model and simple advection model. (a) Sensible heat flux from the full model (W m^{-2}), (b) depth-averaged temperature from full model and estimate (°C), (c) depth-averaged meridional temperature gradient from full model and estimate (10^{-3} °C m^{-1}), and (d) depth-averaged pressure gradient term from full model and estimate (10^{-3} m s^{-2}).

around 2°–3°N with a maximum value of around 0.6°C (100 km)$^{-1}$ for the estimate and 0.9°C (100 km)$^{-1}$ for the full model.

The resultant surface pressure gradient term derived from the hydrostatic approximation shows a maximum of around 0.17×10^{-3} m s^{-2} centered at 2°–3°N (dashed line in Fig. 10d). This may be compared with the full observed and modeled surface pressure gradient term: both reached a maximum of around 0.35 to 0.4×10^{-3} m s^{-2} centered at 3°–4°N (see Fig. 10d, solid line). Part of the difference is due to the neglect of water vapor: the pressure gradient calculated using only the temperature in the full model (Fig. 10d, asterisk) is much closer to the estimate. The other main part of the difference is due to the upper-level pressure gradients in the full model; at 900-m height the gradients reach up to 0.08×10^{-3} m s^{-2} (see Fig. 12).

In summary, the estimated and full pressure gradients are qualitatively similar and both show the spatial lag of between 2° and 4° latitude downstream of the SST gradient (Fig. 8a). The contribution of the thermal advection term, noted in both model and observations, is a feature not accounted for by Lindzen and Nigam (1987) or Wallace et al. (1989) and is important to the behavior of the cross-equatorial flow. In particular, the following section shows that the pressure gradient mechanism that takes this thermal advection effect into account is compatible with the strongest surface wind speeds being located north of the Equatorial Front, as observed.

5. Momentum budget

The PBL is expected to vary in structure across the equator according to the relative importance of terms in the momentum budget. In this section, the model budget will be analyzed in detail to help explain the cross-equatorial flow. First, the surface distribution of momentum budget terms will be shown to explain the surface divergence over the Equatorial Front. The two main balances near the equator are then discussed. Next, the depth-averaged budget is compared with previous, depth-averaged PBL models. Finally, the vertical structure will be used to show how vertical shear of horizontal wind is modified.

The momentum budget may be written in the model coordinates (x, y, σ):

$$\underset{\text{I}}{\frac{\partial \mathbf{u}}{\partial t}} = \underset{\text{II}}{-\mathbf{u}\cdot\nabla\mathbf{u}} \underset{\text{III}}{-\frac{d\sigma}{dt}\cdot\frac{\partial \mathbf{u}}{\partial \sigma}} \underset{\text{IV}}{-f\mathbf{k}\times\mathbf{u}} \underset{\text{V}}{-\{\nabla\Phi + RT_v\nabla \ln(p_s)\}} + \underset{\text{VI}}{K_H\nabla^4\mathbf{u}} + \underset{\text{VII}}{\frac{\partial}{\partial\sigma}\left(\frac{g\sigma}{RT_v}\right)^2 K_V(\sigma)\frac{\partial \mathbf{u}}{\partial\sigma}}, \quad (5a)$$

or equivalently in Cartesian coordinates (x, y, z)

$$\underset{\text{I}}{\frac{\partial \mathbf{u}}{\partial t}} = \underset{\text{II}}{-\mathbf{u}\cdot\nabla\underline{\mathbf{u}}} \underset{\text{III}}{-w\frac{\partial \mathbf{u}}{\partial z}} \underset{\text{IV}}{-f\mathbf{k}\times\mathbf{u}} \underset{\text{V}}{-\frac{1}{\rho}\nabla p} \underset{\text{VI}}{+K_H\nabla^4\mathbf{u}} + \underset{\text{VII}}{\frac{1}{\rho}\frac{\partial}{\partial z}\rho K_V(z)\frac{\partial \mathbf{u}}{\partial z}}, \quad (5b)$$

where Φ is the geopotential, p is pressure, subscript s denotes surface value, $\mathbf{k}$ is a unit vertical vector, t is time, ρ is the air density, g is acceleration due to gravity, R is the ideal gas constant, T_V is the virtual temperature, K_V is the vertical mixing coefficient for momentum, K_H is the horizontal mixing coefficient for momentum, f is the Coriolis parameter, ln is the natural logarithm and $\times$ denotes the cross product, ∇^4 is the biharmonic operator, and other symbols are defined above. Here, term I represents local tendency, term II

the horizontal advection, term III the vertical advection, term IV the Coriolis force, term V the pressure gradient, term VI is horizontal mixing, and term VII is vertical mixing. The coefficient K_V is derived from 1.5-level turbulence closure and cumulus parameterization (see the references in Table 1 for more details), while K_H is deformation and grid spacing–dependent (Table 1).

a. Surface momentum budget

The spatial distribution of the IPRC-RegCM near-surface (z = 26 m) momentum budget is shown in Fig. 11a. The important vector terms of Eq. (5) are shown as arrows (the horizontal mixing term VI was negligible, as was the vertical advection III) as defined in the key. For reference, the SST field is overlaid. The most striking aspect evident from Fig. 11a is that the terms in the Northern Hemisphere are considerably larger than in the Southern Hemisphere. This is because the SST gradient field is asymmetric about the equator with the cold tongue bounded by a weak SST gradient to the south, but with a much stronger gradient to the north. In Fig. 11b, the momentum budget at the equator and to the south is shown in more detail (note the change in scale arrow).

At first glance, the surface momentum budget shows the dominance of two types of balance. South of the equator there is an Ekman balance between Coriolis, pressure gradient, and mixing forces (Fig. 11b), while north of the equator there is a primary balance between pressure gradient and mixing, and the Coriolis term is relatively small (Fig. 11a). These balances are generally consistent with the momentum equations used by Lindzen and Nigam (1987), with the following distinction: the Lindzen–Nigam assumption of collocated pressure and SST anomalies would erroneously place the strongest winds on the SST front; in the present model the strongest winds are north of the SST front where the pressure gradient has a maximum, due to the effect of thermal advection.

A closer inspection of the near-equatorial region (Fig. 11b) reveals a further balance between pressure gradient, advection, and mixing. This is the advective regime discussed by Mahrt (1972). He hypothesized that close to the equator the advective terms become important due to the vanishing of the Coriolis term. Indeed, in Fig. 11b, the advective term at the equator almost replaces the Coriolis term at 4°S in magnitude and direction (e.g., at 96°W). However, there is a huge increase of pressure gradient at the equator relative to that at 2°S that must be compensated for by other terms. We hypothesize that this is done by an increase in mixing term (drag) and a further increase in the advection term. This point will be returned to in the discussion. In general, the advective term and balance are important only within about 1° of the equator.

b. Depth-averaged momentum budget

The momentum budget results from a depth average over the lowest 1 km of the atmosphere were found to be similar to those from the near surface shown in Fig. 11. (Note that the essential balances were insensitive to a choice of averaging depth between 500 and 1200 m approximating the boundary layer depth.) The only significant difference was that the magnitude of all the terms north of the equator was smaller in the depth average relative to the surface budget. This was due to the surface-enhanced pressure gradient and the surface-enhanced drag.

In general, the depth-averaged momentum balance agreed with that observed by McGauley et al. (2004) at 95°W (their Fig. 9). McGauley et al. noted a rapid increase in mixing (sum of the surface drag term and entrainment) at 2°–3°N in the v momentum budget coincident with the largest pressure gradient, consistent with the present model results. They also noted the generally smaller terms in the u component of the momentum balance north of the equator (cf. with Fig. 11a). The effect of PBL top entrainment on the momentum balance is also discussed in de Szoeke and Bretherton (2004) and Stevens et al. (2002).

c. Vertical structure of the momentum budget

This subsection examines the vertical sections of the v momentum budget terms along the line of 95°W to explain the changes of the boundary layer structure across the Equatorial Front. Considering the pressure gradient forcing (Fig. 12, shading), this has a maximum at the surface between 3° and 4°N, as noted above, which reduces with height and reverses sign above 1000 m. The vertical distribution of the pressure gradient agrees reasonably well with that observed by McGauley et al. (2004), with highest values near the surface, greatest at low latitudes, reducing with height, and a sign reversal above 1 km north of 3°N.[3]

The sense of the pressure gradient forcing north of the equator is to accelerate the surface flow and to reduce the surface shear, as observed. Over the cold tongue, there is a local surface minimum of the pressure gradient forcing, so the sense of the forcing here is to enhance the vertical shear, again as observed. In contrast, the vertical mixing term (Fig. 12, contours) generally opposes that of the pressure-driving term, and hence acts in the opposite sense to the observed changes in vertical shear. Consequently, these vertical

[3] Note that the vertical sections of pressure gradient derived from dropsonde data of McGauley et al. (2004) show maximum gradient at the surface at the equator (their Fig. 8d), whereas their estimate of surface pressure gradient from flight-level data showed a maximum at 2°N (their Fig. 4), consistent with our results. The differences may be due to the different times of the dropsonde and flight-level measurements, or instrumental differences (M. McGauley 2004, personal communication).

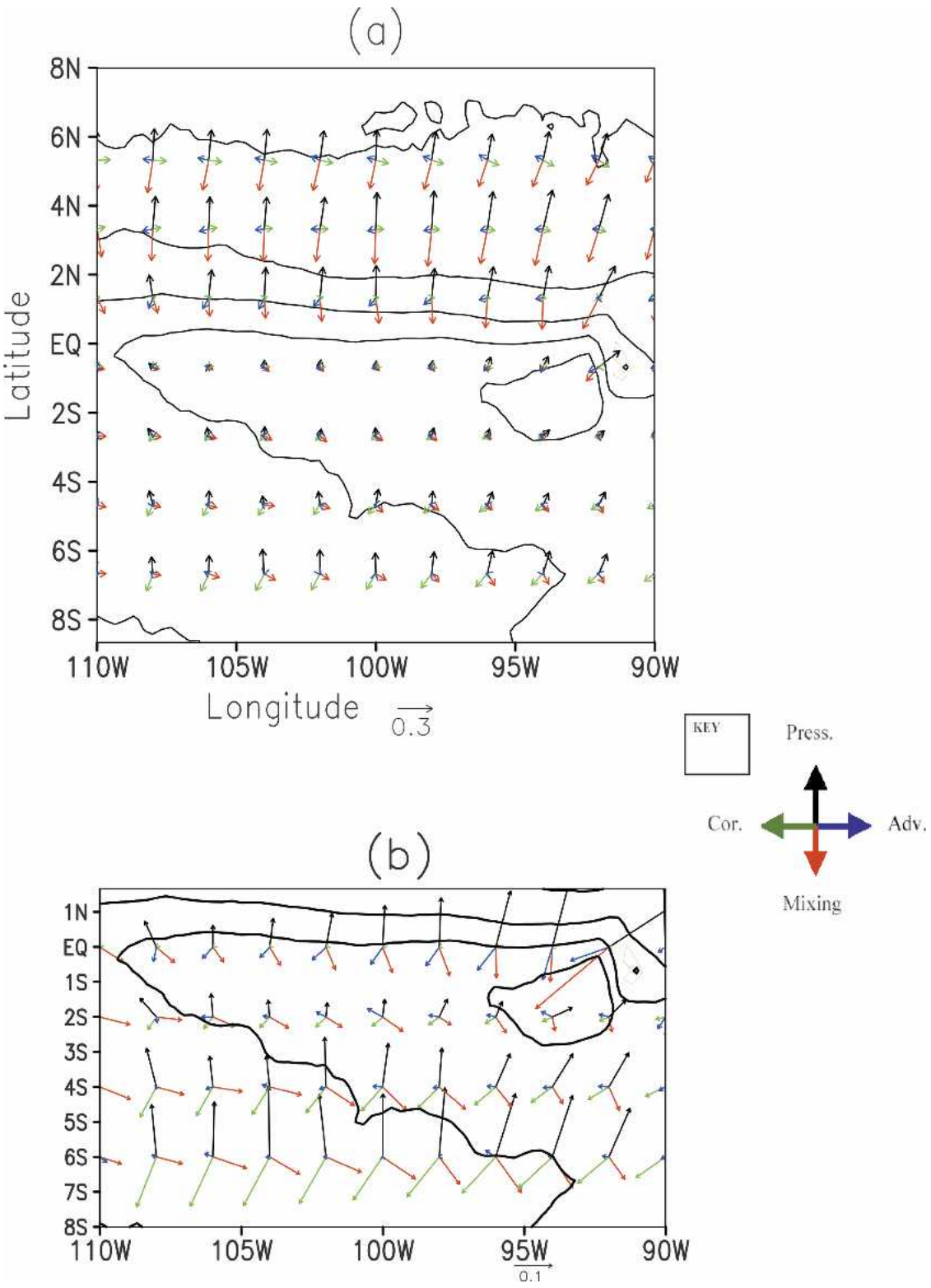

FIG. 11. Balance of momentum budget terms at the lowest model level (a) from 8°S to 8°N, (b) close up of near-surface level between 8°S and 2°N [note the different scale vector in (b)]. All vectors show the tendency in units of 10^{-3} m s^{-2}. Colored vectors represent different terms in (5). (See key: here "Press." denotes the pressure gradient forcing, "Adv." the advective term, and "Cor." the Coriolis term.) The mean SST field is overlaid as a thick black line, with contour intervals of 2 K.

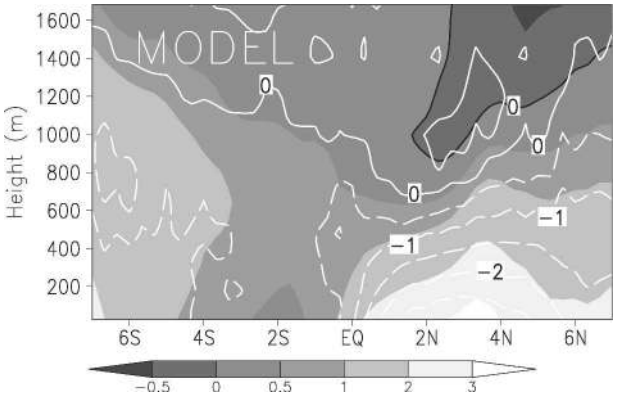

FIG. 12. Vertical section of momentum budget terms at 95°W, with units of 10^{-4} m s^{-2}: pressure gradient driving [term V of (5); shaded], and vertical mixing (term VII; contours, negative values dashed, intervals of 0.5×10^{-4} m s^{-2}).

sections suggest that it is the pressure gradient that acts in the model to change the vertical shear, as seen in Fig. 6.

6. Discussion

This paper has presented simulations that suggest the dominance of pressure gradient force in driving the cross-equatorial flow. This contrasts with the advection hypothesis of Mahrt (1972), Tomas et al. (1999), and the vertical mixing mechanism of Wallace et al. (1989), presented in the introduction.

The difference between the proposed mechanism of this paper and the advective hypothesis lies mainly in the presence of rapid changes in pressure gradient in the regional climate model simulations. In contrast, Mahrt (1972) and Tomas et al. (1999) assumed rather smooth or fixed pressure gradients. The relative importance of the advection term and the pressure gradient term was investigated in a sensitivity experiment. Here the $v\partial u/\partial y$ term, which Tomas et al. (1999) noted as a major contributor to cross-equatorial flow in their model, was removed from the regional climate model simulation. The results showed that, although the advection was significant to the zonal component of the flow, it did not significantly affect the divergence at the Equatorial Front and the location of the strongest meridional winds (results not shown). In the current model, the rapid change in pressure gradient near the equator is the major contributor to the acceleration and divergence, and the maximum pressure gradient at 3°–4°N fixes the position of the strongest winds.

Wallace et al. (1989) suggested that north of the cold tongue the surface layer becomes unstable and the vertical mixing of momentum mechanism dominates, accelerating the surface winds. The present model and the observations from EPIC may also be examined for evidence of this mechanism. For winds to be accelerated at the surface as for the Wallace et al. mechanism, term VII of the momentum budget (5) must be positive near the surface, which is equivalent to a vertical convergence of momentum flux. The model profiles of momentum flux (Figs. 13a,b) over the cold tongue and at 2°N only show divergence of flux in the lower PBL, consistent with mixing acting as a drag on the flow as shown in Fig. 12. In contrast, there is some evidence for convergence of momentum flux from the NCAR C130 measurements near the surface at 0.5°S (Fig. 13c) in the lowest 100 m, but not at 2°N (Fig. 13d). However, it should be noted that the observations and model are not easy to compare: the NCAR C130 flux values at different heights were measured at different times of the day and may not represent a truly synoptic picture of the vertical structure, and the vertical sampling is less at 2°N than at 0.5°S in the flight data and may have missed any near-surface convergence there.

These results suggest that the regional climate model may be missing the additional influence of the Wallace et al. (1989) mechanism at the edge of the cold tongue. This may explain why the model underpredicts the change in shear and surface wind speed compared to the EPIC2001 observations (section 3b). However, farther north over the warmer water at 2°N, both the present model results and the observations suggest that the Wallace et al. mechanism becomes less important than the pressure-driven acceleration.

The results of this study may also be compared with a recent simulation of the cross-equatorial flow by de Szoeke and Bretherton (2004). Using a Lagrangian large eddy simulation (LES) of the boundary layer, driven by large-scale forcing from NCEP, they determined that, although the depth-averaged velocity in the boundary layer was reduced as the SST front was crossed, the surface winds increased due to the vertical transport of momentum, consistent with the Wallace et al. (1989) mechanism. Some differences between the results of de Szoeke and Bretherton and of this present paper can be attributed to the way that pressure effects are included in the models. In the current paper, pressure anomalies are computed by the model, and this allows the pressure anomalies created by the heating of the boundary layer across the front to feed back onto the dynamics. For the de Szoeke and Bretherton simulations, the background pressure gradient is derived from the NCEP–NCAR reanalysis, which exhibits peak (negative) gradients between 2°S and the equator. This contrasts with the present paper's results that surface pressure driving is weakest over the cold tongue and peaks north of the Equatorial Front (corroborated by observations). Hence, the importance of pressure driving is likely to be underestimated in de Szoeke and Bretherton (2004).

7. Conclusions

This paper has analyzed the cross-equatorial flow in the eastern equatorial Pacific using a high-resolution regional climate model. The main aim was to clarify the

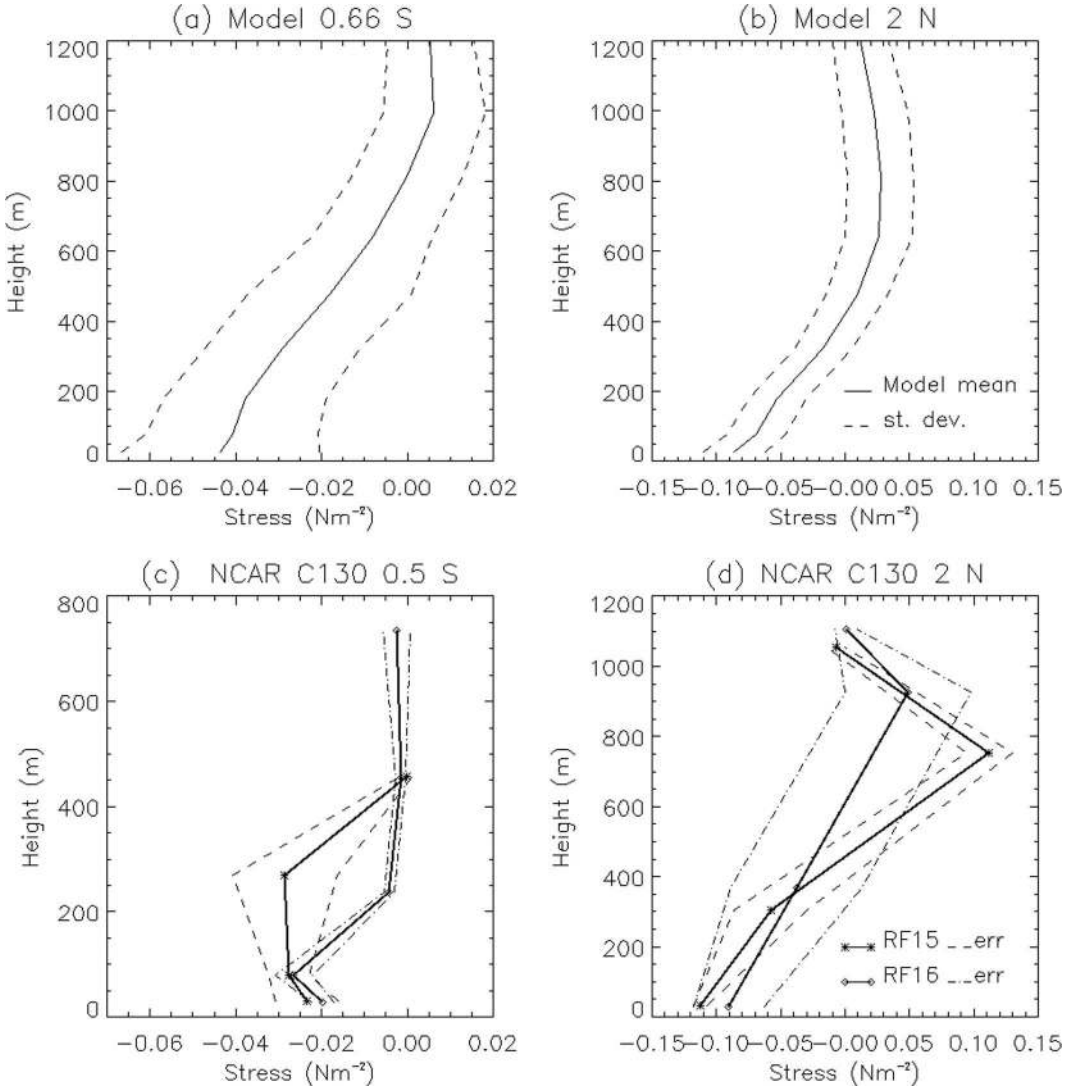

FIG. 13. Vertical structure of meridional stress $\tau_y = \rho\overline{vw'}$ (N m^{-2}) from (a), (b) model simulations and (c), (d) EPIC2001 NCAR C130 flight data, 95°W: (a), (c) at 0.5°S or 0.66°S, (b), (d) at 2°N. In (a), (b) the ±standard deviation envelopes are shown as dashed lines. In (c), (d) thick lines with symbols denote the time mean from several legs at that location and height: lines without symbols indicate the ±1 standard error envelope from the legs. Data are from flight 15 (3 Oct 2001) and flight 16 [5 Oct 2001; see legend in (d)].

relative importance of pressure gradient, vertical redistribution of momentum, and advection to the cross-equatorial flow. The model was compared against detailed in situ and satellite observations, and good qualitative agreement was found in the horizontal and vertical distributions of wind, temperature, humidity, pressure, and cloudiness. The model also agrees well with measurements of the change in surface turbulent fluxes across the SST front, although an overall bias of higher fluxes in the model compared to data was noted.

Analysis of the simulated thermodynamic and momentum budgets elucidated the mechanisms behind the cross-equatorial flow. The thermodynamic balance was found to be dominated by horizontal advection and surface sensible heating across the SST front. This leads to an air temperature perturbation field that spatially lags the SST anomalies and gives rise to a hydrostatic pressure gradient 2° to 3° latitude downstream of the SST front, as observed.

The model shows that the SST front effect on atmospheric temperature and moisture is trapped in the shallow PBL and the associated pressure gradient drives the surface flow, much as envisioned by Lindzen and Nigam (1987). However, while the original Lindzen and Nigam model assumes that PBL air temperature is in equilibrium with local SST, so that SST gradients and pressure-gradient-driven winds are collocated near the

equator, the lagged pressure gradient in our results gives rise to strongest winds downwind and north of the oceanic front, as seen in satellite and in situ data.

A detailed analysis of the momentum budget reveals that air parcels pass through two major regime changes as they cross the equator and the equatorial front. First, as the parcel approaches to within a narrow band (about 1° latitude) of the equator from the south, the balance changes from an Ekman regime to an advective regime. However, the advective regime differs somewhat to that found by Mahrt (1972) and Tomas et al. (1999) due to the presence of an increasing pressure gradient. Here the flow is accelerated and divergence is observed. Second, north of 1°N, the balance transitions into one between pressure gradient and surface drag. In this dominant regime the strongest winds coincide with the largest pressure gradients, located between 3° and 4°N.

At 95°W, the location of the EPIC2001 campaign, the winds are mainly meridional near the equator and change from a sheared profile with low surface wind over the cold tongue to a more uniform profile over the warm water north of the front, both in the model and observations. Investigation of the vertical structure of the momentum budget from the model showed that changes with height of the pressure gradient contribute to the changes in vertical shear of the meridional velocity.

These results demonstrate that pressure gradient force is an $O(1)$ process driving the spatial changes of the cross-equatorial flow, a similar result to that found by Cronin et al. (2003) and Small et al. (2003) with respect to tropical instability waves. Our analysis of the model simulations did not show that vertical redistribution of momentum (Wallace et al. 1989) was acting to enhance the changes in surface wind. In contrast, EPIC2001 flight data showed some possible evidence of this mechanism at work at the equator, but not farther north. If the model is underestimating the importance of this mechanism, this may explain why the change in vertical shear seen across the front is less in the model than observed in EPIC2001.

Large variations in surface winds and associated convergence/divergence are not unique to the Pacific equatorial front but are common to major SST fronts over the world's ocean [see Xie (2004b) for a recent review of relevant satellite observations]. The high-resolution regional models and diagnostics outlined here will be useful in investigating PBL adjustment to such oceanic fronts in the future.

Acknowledgments. The TMI data (version 3) and QuikSCAT data are obtained from the Web site of Remote Sensing Systems. We thank Meghan Cronin, Simon de Szoeke, and Nicolai Thum for providing data and interesting discussion. This study is supported by NASA Grant NAG-10045 and JPL Contract 1216010, NOAA Grant NA17RJ1230, NSF Grant ATM01-04468 and ATM00-02322, and the Japan Agency for Marine–Earth Science and Technology.

REFERENCES

Chou, M., M. J. Suarez, C.-H. Ho, M. M.-H. Yan, and K.-T. Lee, 1998: Parameterizations for cloud overlapping and shortwave single-scattering properties for use in general circulation and cloud ensemble models. *J. Climate,* **11,** 202–214.

Cronin, M. F., S.-P. Xie, and H. Hashizume, 2003: Barometric pressure variations associated with eastern Pacific tropical instability waves. *J. Climate,* **16,** 3050–3057.

——, N. Bond, C. Fairall, J. Hare, M. J. McPhaden, and R. A. Weller, 2002: Enhanced oceanic and atmospheric monitoring underway in Eastern Pacific. *Eos, Trans. Amer. Geophys. Union,* **83,** 205, 210–211.

Davey, M. K., and Coauthors, 2002: STOIC: A study of coupled model climatology and variability in tropical ocean regions. *Climate Dyn.,* **18,** 403–420.

de Szoeke, S. P., and C. S. Bretherton, 2004: Quasi-Lagrangian large eddy simulations of cross-equatorial flow in the east Pacific atmospheric boundary layer. *J. Atmos. Sci.,* **61,** 1837–1858.

——, ——, N. A. Bond, M. F. Cronin, and B. M. Morley, 2005: EPIC 95°W observations of the eastern Pacific atmospheric boundary layer from the cold tongue to the ITCZ. *J. Atmos. Sci.,* **62,** 426–442.

Detering, H. W., and D. Etling, 1985: Application of the E–ε turbulence model to the atmospheric boundary layer. *Bound.-Layer Meteor.,* **33,** 113–133.

Dickinson, R. E., A. Henderson-Sellors, and P. J. Kennedy, 1993: Biosphere–atmosphere transfer scheme (BATS) version 1e as coupled to the NCAR Community Climate Model. NCAR Tech. Note NCAR/TN-387+STR, 72 pp.

Edwards, J. M., and A. Slingo, 1996: Studies with a flexible new radiation code. 1: Choosing a configuration for a large-scale model. *Quart. J. Roy. Meteor. Soc.,* **122,** 689–719.

Fairall, C. W., E. F. Bradley, D. P. Rogers, J. B. Edson, and G. S. Young, 1996: Bulk parameterisation of air-sea fluxes for Tropical Ocean-Global Atmosphere Coupled-Ocean Atmosphere Response Experiment. *J. Geophys. Res.,* **101,** 3747–3764.

Gregory, D., J.-J. Morcrette, C. Jakob, A. C. M. Bejiaars, and T. Stockdale, 2000: Revision of convection, radiation and cloud schemes in the ECMWF integrated forecast system. *Quart. J. Roy. Meteor. Soc.,* **126,** 1685–1710.

Kalnay, E., and Coauthors, 1996: The NCEP/NCAR 40-Year Reanalysis Project. *Bull. Amer. Meteor. Soc.,* **77,** 437–471.

Langland, R. H., and C.-S. Liou, 1996: Implementation of an E-ε parameterization of vertical subgrid-scale mixing in a regional model. *Mon. Wea. Rev.,* **124,** 905–918.

Lindzen, R. S., and S. Nigam, 1987: On the role of sea surface temperature gradients in forcing low level winds in the Tropics. *J. Atmos. Sci.,* **44,** 2418–2436.

Mahrt, L. J., 1972: A numerical study of advective accelerations in an idealized low latitude planetary boundary layer. *J. Atmos. Sci.,* **29,** 1477–1484.

Mailhot, J., and R. Benoit, 1982: A finite element model of the atmospheric boundary layer suitable for use with numerical weather prediction schemes. *J. Atmos. Sci.,* **39,** 2249–2266.

McGauley, M., C. Zhang, and N. A. Bond, 2004: Large-scale characteristics of the atmospheric boundary layer in the eastern Pacific cold tongue—ITCZ region. *J. Climate,* **17,** 3907–3920.

Mesocho, C. R., and Coauthors, 1995: The seasonal cycle over the tropical Pacific in general circulation models. *Mon. Wea. Rev.,* **123,** 2825–2838.

Nordeng, T. E., 1994: Extended versions of the convective parameterisation scheme at ECMWF and their impact upon the mean climate and transient activity of the model in the Trop-

ics. Research Dept. Tech. Memo. 206, ECMWF, Shinfield Park, Reading RG29AX, UK.

Raymond, D. J., S. K. Esbensen, M. Gregg, and C. S. Bretherton, 2004: EPIC2001 and the coupled ocean–atmosphere system of the tropical east Pacific. *Bull. Amer. Meteor. Soc.,* **85,** 1341–1354.

Slingo, A., and H. M. Schrecker, 1982: On the shortwave radiative properties of water clouds. *Quart. J. Roy. Meteor. Soc.,* **108,** 407–426.

Small, R. J., S.-P. Xie, and Y. Wang, 2003: Numerical simulation of atmospheric response to Pacific tropical instability waves. *J. Climate,* **16,** 3722–3740.

Stevens, B., J. Duan, J. C. McWilliams, M. Munnich, and J. D. Neelin, 2002: Entrainment, Rayleigh friction, and boundary layer winds over the tropical Pacific. *J. Climate,* **15,** 30–44.

Sun, Z., and L. Rikus, 1999: Improved application of exponential sum fitting transmissions to inhomogeneous atmosphere. *J. Geophys. Res.,* **104,** 6291–6303.

——, and K. Shine, 1994: Studies of the radiative properties of ice and mixed phase clouds. *Quart. J. Roy. Meteor. Soc.,* **120,** 111–137.

Tiedtke, M., 1989: A comprehensive mass flux scheme for cumulus parameterization in large-scale models. *Mon. Wea. Rev.,* **117,** 1779–1800.

Tomas, R. A., J. R. Holton, and P. J. Webster, 1999: The influence of cross-equatorial pressure gradients on the location of near-equatorial convection. *Quart. J. Roy. Meteor. Soc.,* **125,** 1107–1127.

Vickers, D., and L. J. Mahrt, 2003: The cospectral gap and turbulent flux calculations. *J. Atmos. Oceanic Technol.,* **20,** 660–672.

Wallace, J. M., T. P. Mitchell, and C. Deser, 1989: The influence of sea surface temperature on surface wind in the eastern equatorial Pacific: Seasonal and interannual variability. *J. Climate,* **2,** 1492–1499.

Wang, Y., 1999: A triply nested movable mesh tropical cyclone model with explicit cloud microphysics. Bureau of Meteorology Research Centre Rep. No. 74. [Available from BMRC, GPO Box 1289K, Melbourne, Australia.]

——, 2001: An explicit simulation of tropical cyclones with a triply nested movable mesh primitive equation model: TCM3. Part 1: Model description and control experiment. *Mon. Wea. Rev.,* **129,** 1370–1394.

——, O. L. Sen, and B. Wang, 2003: A highly resolved regional climate model and its simulation of the 1998 severe precipitation events over China. Part I: Model description and verification of simulation. *J. Climate,* **16,** 1721–1738.

Wentz, F. J., and D. K. Smith, 1999: A model function for the ocean normalized radar cross-section at 14 GHz derived from NSCAT observations. *J. Geophys. Res.,* **104,** 11 499–11 514.

Xie, S.-P., 2004a: The shape of continents, air–sea interaction, and the rising branch of the Hadley circulation. *The Hadley Circulation: Past, Present, and Future*, H. F. Diaz and R. S. Bradley, Eds., Springer-Kluwer Academic, 121–152.

——, 2004b: Satellite observations of cool ocean–atmosphere interaction. *Bull. Amer. Meteor. Soc.,* **85,** 195–208.

Xu, K.-M., and D. A. Randall, 1996: A semi-empirical cloudiness parameterization for use in climate models. *J. Atmos. Sci.,* **53,** 3084–3102.